材料研究与应用　2024,18(6):916-933
Materials Research and Application
http://mra.ijournals.cn
Email:clyjyyy@gdinm.com

DOI:10.20038/j.cnki.mra.2024.000606

电催化CO_2还原的原位谱学研究进展

王俊,陈腾飞,巨文博*
(华南理工大学物理与光电学院,广东 广州 510640)

摘要: 可再生电力驱动的电催化二氧化碳还原反应(CO_2RR)能将CO_2转化为具有经济价值的燃料和化学品,是实现"碳闭环",达成"碳达峰"和"碳中和"的关键技术。CO_2RR产物之一的甲酸(HCOOH)经济附加值是重要评价因素,以低耗能、高价值而获得学术和产业界的广泛关注。由于p区金属(如锡、铋、铟、和铅)能以高法拉第效率催化CO_2RR而产生HCOOH,因此探究其催化机理和反应活性位点,能够为研发实用型催化剂和优化反应环境提供重要基础支撑。总结了原位观测技术在研究p区金属催化CO_2RR机理和活性位点中的应用,常用的原位观测技术包括拉曼光谱、红外吸收光谱、X射线吸收谱和差分电化学质谱,借助原位观测技术不仅可以分析催化剂表面的化学成键、分子结构、结晶度等信息,还能在电位动态扫描过程中以毫秒的时间分辨对电化学反应产生的气态或易挥发产物,从而进行定性或定量分析。通过原位观测或工况条件下获取的实验数据确认CO_2RR的催化成分,构建反应路径图,为进一步设计高性能、高稳定性的催化剂提供了必要条件。此外,合金化是改良催化剂性能的主要策略之一,简要讨论了p区金属合金化对电子结构、表面性质、催化效果的影响。通过总结原位观测技术对在p区金属催化研究的重要作用,为CO_2RR工程化发展提供坚实基础和创新思路。

关键词: p区金属;二氧化碳还原;甲酸;原位观测技术;拉曼光谱;红外吸收光谱;X射线吸收谱;差分电化学质谱

中图分类号:TB332　　**文献标志码:**A　　**文章编号:**1673-9981(2024)06-0916-18

引文格式:王俊,陈腾飞,巨文博. 电催化CO_2还原的原位谱学研究进展[J]. 材料研究与应用,2024,18(6):916-933.
WANG Jun,CHEN Tengfei,JU Wenbo. Research Progress of Operando Spectroscopy for Electrocatalytic CO_2 Reduction[J]. Materials Research and Application,2024,18(6):916-933.

0　引言

人类于工业革命后大规模使用化石燃料,导致大气中二氧化碳(CO_2)含量不断上升。截至2023年底,大气中CO_2含量已升至约422 ppm[1],超过18世纪中叶之前一万年大气中CO_2含量(约280 ppm)的1.5倍,由此引发全球变暖和海水酸化等环境问题,威胁人类生存和生态稳定[2-4]。依赖自然界的"碳循环"已无法有效地控制大气中CO_2含量,迫切需要技术创新,实现人工"碳循环",进而达到"碳中和"的可持续发展目标[5]。可再生能源驱动CO_2转化为燃料或附加值高的化学品,正在成为人工"碳循环"的重要技术板块[6]。电化学CO_2还原反应(CO_2 reduction reaction, CO_2RR)是电驱动CO_2在电解池内发生脱氧或加氢的过程,其既能固碳又能储能,被认为是理想的"碳循环"技术,获得广泛关注和密集研究[7]。图1为碳循环示意图[8]。

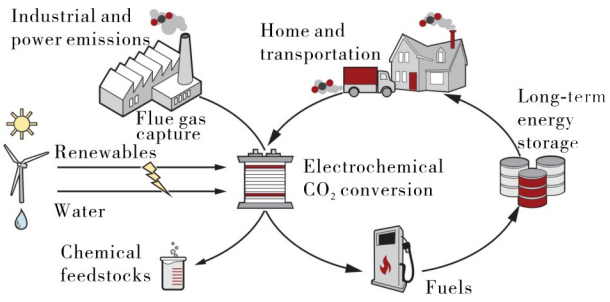

图1　碳循环示意图[8]

Figure 1　Schematic depiction of carbon cycle

电化学CO_2RR的反应机理、催化机制、反应条件因素等基础问题已被逐步解决。已报道的CO_2RR产物多达17种[9],主要产物的热力学平衡电位列于表1[10]。尽管CO_2RR生成的甲烷(CH_4)、乙烯(C_2H_4)、甲醇(CH_3OH)等有机小分子产物的热力学平衡电位更高,但受限于多电子迁移的复杂性和

收稿日期:2024-09-28
基金项目:国家自然科学基金项目(12104164);广东省基础与应用基础研究基金项目(2024A1515012342);广州国家实验室专项项目(GZNL2023A03006)
作者简介:王俊,硕士研究生,研究方向为表面和界面物理。E-mail:202320130264@mail.scut.edu.cn。
通信作者:巨文博,博士,教授,研究方向为表面和界面物理及电磁功能材料。E-mail:wjuphy@scut.edu.cn。

缓慢的碳氢(C—H)成键过程,此类产物的选择性和能量效率都较低[11]。然而,CO_2RR生成的一氧化碳(CO)或甲酸(HCOOH)产物的两电子($2e^-$)迁移过程更容易发生。单金属催化剂有不同的CO_2RR产物。例如:金(Au)[12]或银(Ag)[13]单金属催化剂,催化CO_2RR生成CO;p区金属(p-Block metals),如锡(Sn)、铟(In)、铅(Pb)、铋(Bi)等,催化CO_2RR生成HCOOH[14];铜(Cu)是最特殊的单金属催化剂,能催化CO_2RR生成烃、烯、醇等有机小分子[15-16]。技术的经济性分析表明,电催化CO_2RR生成的HCOOH具有能耗密度低且经济价值高的优势[17],因此该技术路线最具工程化价值,由此推动了p区金属催化剂在CO_2RR中的工作机制和优化策略研究。Pander等[18]指出,p区金属能催化CO_2RR生成HCOOH,但催化活性物和反应机制存在显著差异,如Sn和In被视为依赖表面氧化物的催化剂,而Bi和Pb则不依赖于表面氧化物。p区金属催化剂在CO_2RR中存在相转换和形貌演化等现象[19],使非原位研究方法遭遇了前所未有的挑战。原位或现场原位分析催化界面状态,并关联其表现,是确定活性成分和揭示催化机理的必要方法[20]。

表1 CO_2RR主要产物的热力学平衡电位表(vs. RHE, pH=7)[10]

Table 1 Thermodynamic equilibrium potentials of CO_2RR main products (vs. RHE, pH=7)

序号	半反应式	电位/V
1	$CO_2+e^-\rightarrow CO_2^-$	−1.49
2	$CO_2+2H^++2e^-\rightarrow CO+H_2O$	−0.11
3	$CO_2+2H^++2e^-\rightarrow HCOOH$	−0.20
4	$CO_2+4H^++4e^-\rightarrow HCHO+H_2O$	−0.10
5	$CO_2+6H^++6e^-\rightarrow CH_3OH+H_2O$	0.03
6	$2CO_2+9H_2O+12e^-\rightarrow CH_3CH_2OH+H_2O$	−0.77
7	$CO_2+8H^++8e^-\rightarrow CH_4+H_2O$	0.17
8	$2CO_2+14H^++8e^-\rightarrow C_2H_6+4H_2O$	0.14
9	$2CO_2+12H^++12e^-\rightarrow C_2H_4+4H_2O$	0.07
10	$2H^++2e^-\rightarrow H_2$	0.00

本综述聚焦p区金属催化剂在CO_2RR生成HCOOH过程中的基础问题,着重探讨原位或现场原位表征技术在基础研究中的应用。首先,介绍常用的电化学耦合现场原位表征技术,包括拉曼光谱(Raman spectroscopy, RS)、红外吸收光谱(Infrared absorption spectroscopy, IRAS)、X射线吸收谱(X-ray absorption spectroscopy, XAS)和差分电化学质谱(Differential electrochemical mass spectroscopy, DEMS)。其次,介绍现场原位表征技术研究p区金属催化CO_2RR的典型案例,以及形成的重要结论。同时,结合理论计算,分析催化活性位点、反应中间产物及反应动力学。基于已有知识,简要讨论p区金属合金化策略带来的性能改变和可能的优化路径。最后,总结电催化CO_2RR技术存在的挑战并予以展望。

1 原位表征技术

电势能驱动物质偏离化学平衡态是电化学过程发生的必要条件。电催化材料,尤其是非贵金属类材料,在电势能驱动下发生成分或结构演化,产生了有别于稳定状态的新物质。非原位表征技术将无法准确描述催化剂的成分和结构信息,迫切需要在研究过程中引入多种原位或现场原位分析表征手段以获取催化剂的动态信息,为探究反应机理和优化催化剂性能提供可靠的实验支撑[20-22]。简要介绍了4种常用于电化学研究的现场原位表征技术,包括拉曼光谱(RS)、红外吸收光谱(IRAS)、X射线吸收谱(XAS)、差分电化学质谱(DEMS)。此外,还有多种材料表征技术可用于现场原位分析,此文中不再逐一介绍。

1.1 拉曼光谱(RS)

RS基于物质对光子的非线性散射,能够探测分子的特征振动或转动模式,进而获取物质的化学成键、分子结构、结晶度等信息[23]。现场原位RS不仅能提供催化剂在实际工况下的成分和结构信息,还能揭示反应物在临近界面的浓度梯度,以及催化剂表面吸附的中间产物[24]。RS与IRAS都是分子振动谱,在应用中互为补充,如对称分子的对称振动可以被RS检出,极性基团、非对称分子或对称分子的不对称振动可以被IRAS检出[25]。由于水分子具有较低的拉曼散射截面,现场原位RS适用于含水电

解液内电化学界面的表征。

Ren等[26]于2000年报道了适用于共聚焦拉曼光谱仪的电化学反应器(见图2[27]),并用现场原位RS观测甲醇(CH_3OH)在铂(Pt)电极表面的电催化氧化过程。Yeo等[28-30]于2010年开发了物镜浸润式现场原位RS系统,用厚13 μm的透明特氟龙薄膜包裹着共聚焦拉曼光谱仪物镜,并通过浸入电解液的物镜高效收集微弱的拉曼散射光以获得更高的探测灵敏度,观测到金(Au)电极表面氧析出反应(Oxygen evolution reaction, OER),以及存在表面吸附的过氧化氢中间产物(—OOH)[28],并且发现Au衬底表面氧化钴(CoO_x)催化剂具有更丰富的Co^{IV}核心,从而显著提升了OER催化活性[29],否定了氧化镍(NiO_x)催化剂中β-NiOOH是OER催化活性物质,指出一种价态未知的镍基氧化物已先于OER形成[30]。然而,以上现场原位RS系统均无法避免显微物镜与电极间距过小(通常为0.2 mm)造成的质量输运干扰问题。2016年,Zeng等[31]提出了一种全新的现场原位RS物镜设计方法,采用水滴浸润物镜和石英玻璃窗口的间隙,通过全光路折射率匹配,将电极到石英玻璃窗口的间距显著提升到2 mm以上。至此,现场原位RS系统已经能采集到高质量的电极表面拉曼光谱,为电催化过程的原位谱学研究提供了充足的技术准备。尽管如此,现场原位RS的广泛应用仍有巨大挑战,如物质对光子的拉曼散射截面较小,仅为瑞利散射截面的1×10^{-6}—1×10^{-8}。为了增强拉曼信号,发展出了表面增强拉曼散射(Surface-enhanced Raman scattering, SERS)、针尖增强拉曼散射(Tip-enhanced Raman scattering, TERS)、表面隔离纳米颗粒增强拉曼散射(Shell-isolated nanoparticle-enhanced Raman scattering, SHINERS)等技术,将拉曼信号提升至高1×10^{15}倍[21, 32-34],极大提升了拉曼光谱的分析灵敏度。Tafazoli等[35]利用SERS发现了$Cu_2(CO_3)(OH)_2$,并认为该物质与电极表面吸附CO有强相关,解释了两种Cu氧化物电催化CO_2RR生成C_2产物存在差异性的原因。

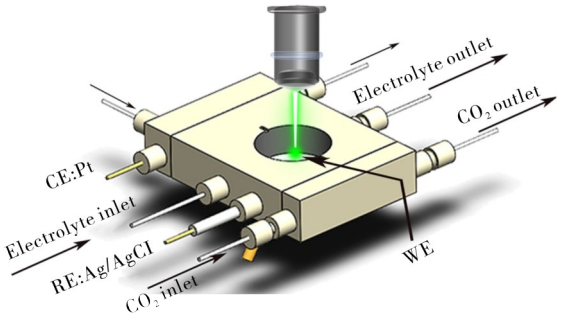

图2 现场原位RS电化学反应装置示意图[27]

Figure 2 Schematic depiction of operando RS electrochemical reaction device

1.2 红外吸收谱(IRAS)

IRAS是分子在共振频率对红外光的选频吸收谱,能分析分子结构和化学键,以及凝聚态物质的构象和构型[36]。IRAS原位观测电化学过程面临两大挑战,即水性电解液在红外波段强吸收且吸收能力变化大,红外光在催化界面的吸收量占全光路总吸收量的比例太低。因此,导致红外光直接穿透电解液进行原位观测的技术路径不可行。为解决以上问题,需对电化学反应池进行不断地改进,以实现现场原位IRAS分析。Moss等[37]于1990年报道了透射型现场原位IRAS电化学反应池,该反应器以Au网为工作电极并被两片CaF_2窗口夹在中间,电解液薄层浸润工作电极。透射型现场原位IRAS被成功应用于生物分子在电化学演化过程中,如观测光敏蛋白Photosystem II中非血红素Fe中心与Mn_4CaO_5团簇的长距作用[38],以及Co^{II}卟啉酮的氧化还原过程[39]. 然而,该设计的缺点也不可忽视,即Au网遮挡了红外光,导致光通量过低。Dai等[40]用硼掺杂金刚石电极取代了Au网以提升红外光通量,但是红外光通过电解液后光谱信噪比仍然偏低,以至于透射型现场原位IRAS策略没有广泛推广。Alwis等[41]首先提出了外反射型现场原位IRAS电化学反应池,红外光入射CaF_2窗口并被工作电极表面反射后,被红外探测器接收,该构型中红外光仍需通过电解液薄层,从而造成光信号损失。Liu等[42]利用Au电极表面等离子激元共振,实现了表面增强红外吸收谱(Surface enhanced infrared absorption spectroscopy, SEIRAS)。为了彻底排除电解液对红外光谱的干扰,衰减全反射(Attenuated total reflection, ATR)构型被用于电化学池设计,并已成为主流[43],示意图如图3所示[44]。ATR晶体一般是Ge、ZnSe、金刚石等[45]。红外光聚焦于ATR晶体的内表面,当入射角大于临界角时,红外光在ATR晶体内发生全发射。Kretschmann等[46]于1971年提出了ATR表面增强红外吸收谱(ATR-SEIRAS)技术,在ATR晶体表面沉积金属薄层以实现红外信号增强。金属薄层可用作电极,实现现场原位IRAS在电化学过程中的应用。例如,C—O振动具有较大的红外吸收截面[44],是CO_2RR过程中常被现场原位IRAS检测的中间体。此外,*COOH也具备较强的红外活性,利用原位红外光谱研究*CO,*COOH等中间体能揭示CO_2RR的反应机制及动力学[47-52]。

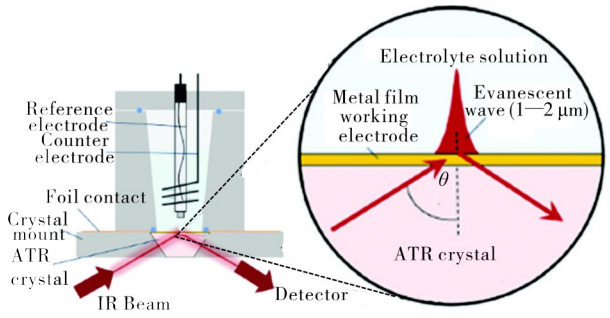

图3 现场原位ATR-IRAS电化学反应装置示意图[44]

Figure 3 Schematic depiction of Operando ATR-IRAS electrochemical reaction device

1.3 X射线吸收谱(XAS)

XAS以同步辐射装置提供的高强度、可调波长X射线为入射光源,通过物质对X射线的特征吸收谱线,分析物质的空间结构和电子态[53],图4为其装置示意图。当电子能被X射线激发跃迁至最低非占据态时,即达到了X射线吸收阈值,随着X射线能量提升而获得吸收边缘曲线[54]。随着金属在费米能级以上的非占据态密度迅速增加,其X射线吸收边缘通常表现为弧正切线型。绝缘体的X射线吸收阈值受到束缚核心激子(电子/空穴对)的影响,在前边缘区域存在具有洛伦兹线型的吸收特征,当X射线能量超过核心激子的结合能时吸收会急剧增加,标志着电子被激发至最低非占据态[55]。X射线吸收的近边缘结构(X-ray absorption near edge structure, XANES)能够获取核心电子跃迁到准束缚瞬态时的形状共振信息[56],通过形状共振谱线强度和宽度分析准束缚瞬态的寿命,以及其与背景态的耦合程度,进而获取物质的电子结构和化学环境信息。物质吸收高能量区间X射线的行为,可以用扩展X射线吸收精细结构(Extended X-ray absorption fine structure, EXAFS)描述。位于非占据态的激发电子在临近原子发生散射相互作用,引起X射线吸收谱存在振荡结构,即EXAFS。通过分析EXAFS,能够了解原子间距和局域的环境信息[57]。现场原位XAS电化学反应装置图如图4所示[54]。利用XAS原位观测电催化过程,能够分析催化剂的空间结构、电子态等随化学环境的演化,也能获取吸附中间产物的近邻配位结构信息[58]。Weng等[59]利用EXAFS原位分析CuPc(Copper^{II}-porphyrin, 卟啉铜)、HKUST-1和Cu(cyclam)Cl_2的Cu基复合材料在CO_2RR过程中的重整,结果表明仅有CuPc在还原电压下会形成Cu纳米簇,因金属Cu可提供催化活性位点。Mistry等[60]利用O_2或H_2等离子体处理金属Cu电极,获得不同氧化层厚度,结果发现使用功率20 W的O_2等离子体处理2 min后,Cu电极在CO_2RR中展现出对乙烯的60%高选择性。通过现场原位XAS实验,揭示了Cu_2O在15 min反应过程中始终存在,并且Cu_2O在表层更加稳定,证实了Cu^+为提高C_2H_4产率的关键物质。

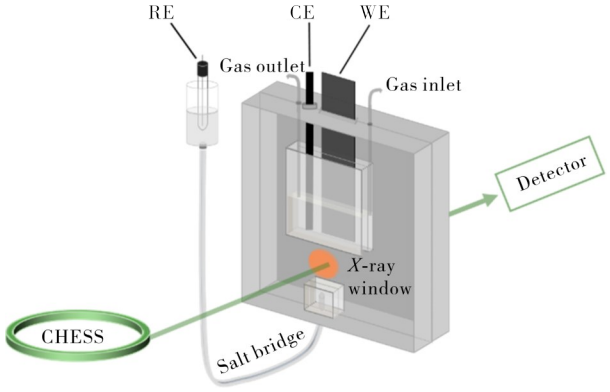

图4 现场原位XAS电化学反应装置示意图[54]

Figure 4 Schematic depiction of operando XAS electrochemical reaction device

1.4 差分电化学质谱(DEMS)

DEMS是将电化学反应池与质谱仪联用的技术,在电位动态扫描过程中能以毫秒的时间分辨率对电化学反应产生的气态或易挥发产物进行定性或定量分析[61-64]。质谱仪需从电极临近空间高效地收集反应产物,因此其探头前端的膜界面被精巧设计,关键参数包括孔隙率、厚度、膜或电极面积,以及催化剂的载荷和界面和电极之间的物理距离等[65]。多孔聚四氟乙烯(Polytetrafluoroethylene, PTFE)因优良的机械稳定性、疏水性、耐酸碱腐蚀性,常用作DEMS的探头膜界面[66]。常用的DEMS反应池如图5所示[67]。

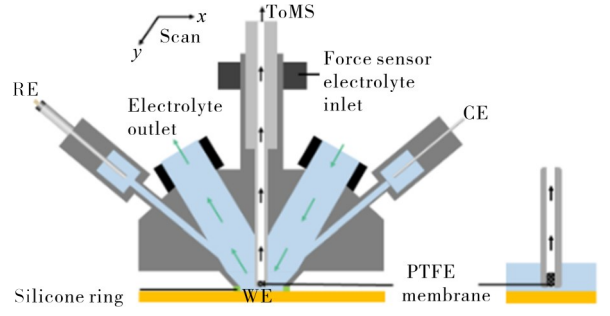

图5 DEMS反应器示意图[67]

Figure 5 Schematic depiction of DEMS, sourced from reference

DEMS常用于分析可检测产物的起始生成电位,并定量分析多种产物的浓度;,通过结合电化学分析结果,可评价不同产物的法拉第效率(Faraday efficiency)。Wang等[64]利用毫秒级分辨率的DEMS,追踪了CuO纳米片催化CO_2RR产生多种产物的起始电位,结果发现:在最初的1 h内(约10圈循环伏安),C_2H_4的起始生成电位从最初的(−0.57±0.07) V(vs. RHE)变负为(−0.63±

0.09) V,而在9 h反应后(约100圈循环伏安)电位变为(−0.77±0.02) V,与此同时,CO的起始生成电位从最初的(−0.38±0.08) V,先变为(−0.48±0.05) V后,维持在变为(−0.48±0.03) V。这种转变归因于Cu表面活性位点减少,还原电压的偏移量表示启动*CO中间产物二聚化生成C_2H_4所需的能量,偏移量越大所需的能量越多。与之相对的,CH_4和乙醇(CH_3CH_2OH)的起始生成电位在9 h反应内基本稳定在−0.8 V至−0.9 V之间,表明可能存在一个控制CH_4和CH_3CH_2OH起始电位的共同反应,并且该机制与前期报导的机理相反。由于CH_4和CH_3CH_2OH拥有相似的起始电位与负相关的法拉第效率,表明CH_4和CH_3CH_2OH拥有共同的还原前驱体。

2 p区金属基催化剂

用于电催化CO_2RR的p区金属主要为Sn、In、Bi和Pb,其金属或氧化物能选择性催化CO_2生成甲酸根($HCOO^-$)或HCOOH,且法拉第效率极高。以气态CO_2为反应物的气体扩散电极,或以CO_2饱和水溶液为反应环境的浸润式电极,获得的法拉第效率均大于90%[14]。由于p区金属基催化剂极具工程化潜力,吸引了大量基础性和应用性的研究,因此原位分析方法在p区金属催化剂的基础研究中被广泛应用。

2.1 Sn基催化剂

Sn基材料用于电催化CO_2RR可追溯至1994年,由Hori等[14]报道的金属Sn电极在CO_2饱和的0.1 mol·L^{-1}的$KHCO_3$溶液中电解CO_2生成$HCOO^-$。通过计算*OCHO中间产物在几种典型金属电极表面的结合能,发现Sn对*OCHO的吸附能适中,既不会因为吸附太弱而无法有效催化反应发生,也不会因为吸附过强造成催化剂表面毒化。因此,Sn位于生成HCOOH反应的火山图[68]顶点位置,是理想的电催化CO_2RR产HCOOH催化剂,因而受到广泛关注和密集研究[27, 47, 69-71]。金属Sn在空气中可自发氧化生成Sn基氧化物(SnO_x),而电催化CO_2RR的还原电位较负,不可避免地引起SnO_x还原,该过程对催化剂表面成分及结构有决定性作用。催化剂演化过程中的催化选择性及活性也是重要科学问题,吸引了大量科研工作者致力于研究SnO_x演化与电催化CO_2RR表现的内在关系[72-77]。因此,原位观测技术在这一课题中发挥了积极且关键的作用。

金属Sn表面在空气中易被氧化为SnO_x,如氧化亚锡(SnO)、氧化锡(SnO_2)等。若CO_2RR发生在pH中性的CO_2饱和$KHCO_3$溶液中,Pourbaix图显示随着电极电势下降,SnO_x会从开路电位的SnO_2还原至SnO,直至金属Sn。SnO_2与Sn的标准电极电势为−0.117 V (vs. NHE)[78],略高于CO_2RR的起始电势。因此,早期的研究普遍假设金属Sn是CO_2RR的活性位[14]。然而,Pourbaix图给出的标准电极电势仅考虑了反应的热力学因素,而忽略了动力学对电极电势的影响。部分亚稳态金属氧化物在低于平衡电位的条件下仍能存在[79],对催化反应过程起到关键作用。2012年,Chen等[80]发现了Sn电极的表面氧化状况对CO_2RR的法拉第效率有显著影响。表面氧化层未被处理的Sn电极,能有效抑制氢析出反应(Hydrogen evolution reaction, HER),使CO_2RR的法拉第效率高达90%以上;而Sn电极表面氧化层被酸刻蚀后,反应电流密度大幅提升,但产物以氢气(H_2)为主,CO_2RR产HCOOH的法拉第效率甚至不及1%。如此显著的差异,明确指向了SnO_x在CO_2RR中起到关键作用,尤其是抑制HER,进而提升CO_2RR的法拉第效率,以及负偏压下依然有SnO_x存在于Sn电极表面,虽与热力学观点不符,但也暗示存在某种动力学过程阻碍了SnO_x的进一步还原。

2015年,Baruch等[48]利用现场原位ATR-IRAS,观测到SnO_x稳定存在于CO_2RR所需的负偏压条件。首先电极表面的SnO_2从Sn^{4+}被还原为Sn^{2+},然后与CO_2结合形成Sn-CO_3中间产物,该中间产物对应于1 500和1 385 cm^{-1}的红外吸收峰,与单齿Sn-CO_3的特征峰一致(见图6(a))。结合相同电位下CO_2RR的电流密度和法拉第效率数据,发现Sn^{2+}是CO_2RR催化活性位点,反应机制如图6(b)所示。Dutta等[81]通过现场原位RS,观测到在CO_2RR过程中Sn电极表面成分的演化过程,参考变量包括反应时长、电极电势和溶液pH(见图7)。从图7(a)和(b)可见,以Sn^{4+}关联的A_{1g}拉曼峰为参考指标,其相对强度经历了两阶段的下降。在pH为8.5的电解液中,随着电极电势由−0.2 V降至−0.8 V (vs. Ag/AgCl)时,A_{1g}峰强度从100%降至约75%;随着电极电势由−1.1 V降至−1.4 V时,A_{1g}峰强度进一步下降至0%。A_{1g}拉曼峰强度变化趋势与CO_2RR产HCOOH的法拉第效率高度一致,即Sn^{4+}部分还原后HCOOH的法拉第效率接近75%,而Sn^{4+}完全还原至Sn^0后HCOOH的法拉第效率也降低至约25%。Sn基电极催化CO_2RR产HCOOH的最高法拉第效率是当SnO_2被部分还原时,并且该结论在3种不同pH的碱性溶液中均成立。因此,SnO_x是电催化CO_2RR产HCOOH的活性成分。Dutta等[50]采用现场原位RS和XANES继续进一步对SnO_x的可能成分进行分析,明确了SnO_2→SnO→Sn的还原过程。SnO的A_{1g}振动模式对应于218 cm^{-1}

的拉曼峰,其峰值在−0.6 V(vs. Ag/AgCl)时开始上升,并在−1.1 V时达到最大,同时HCOOH的法拉第效率始终保持在70%以上。当电极电势持续降低至−1.55 V时,SnO_2和SnO对应的拉曼峰均逐渐消失,表明电极表面已经完全金属化,同时HCOOH的法拉第效率也降至约25%。原位XANES实验结果(见图7(c))与该结论相一致。说明,Sn^{2+}是反应活性位点,并且Sn基催化剂只能在一定电势范围内保持较高的HCOOH法拉第效率,当金属Sn生成时HER将不可避免地主导反应过程。

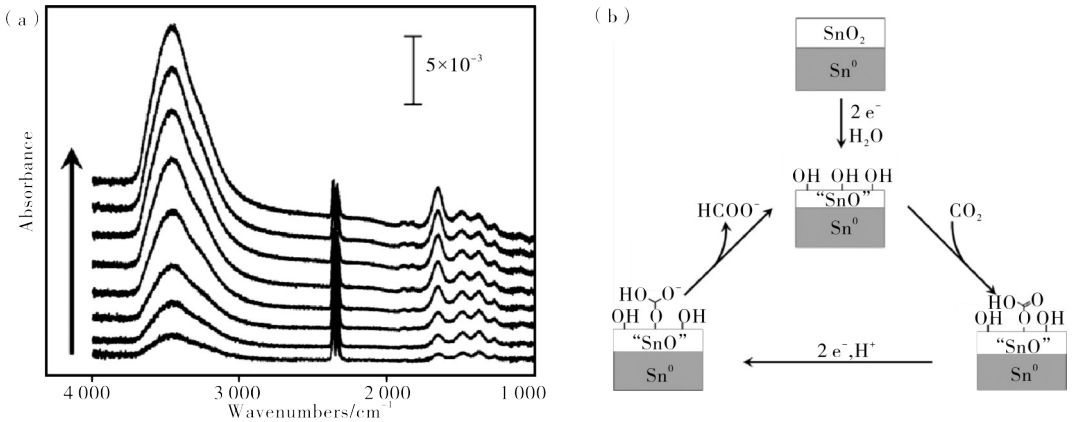

(a)—SnO_x的ATR-IRAS数据;(b)—SnO_x催化CO_2RR的反应机理示意图。

(a)—operando ATR-IRAS data of SnO_x; (b)—schematic depiction of the reaction mechanism of SnO_x catalyzed CO_2RR.

图6 SnO_x的ATR-IRAS谱图及CO_2RR的反应机理示意图[48]

Figure 6 ATR-IRAS spectra of SnO_x and schematic diagram of the reaction mechanism of CO_2RR

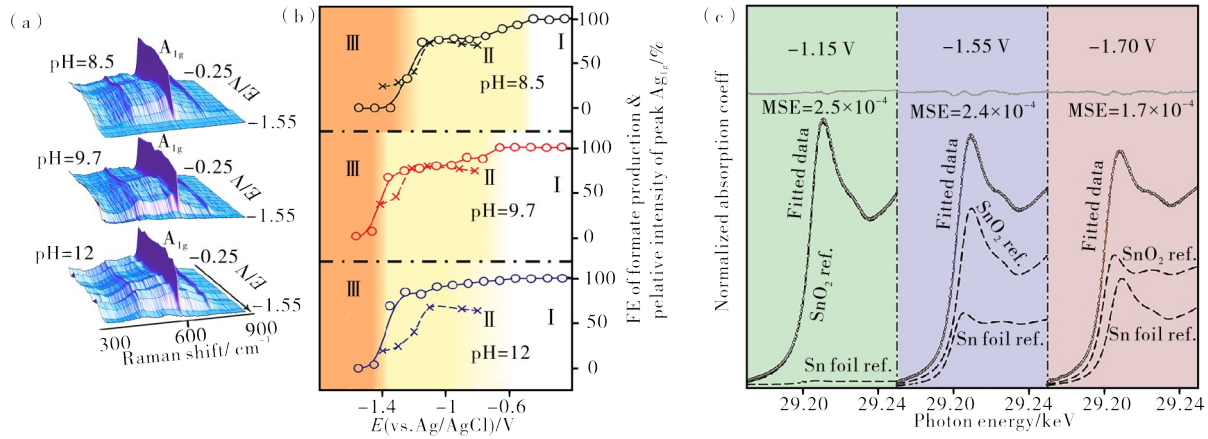

(a)—SnO_2电极表面成分演化过程的原位Raman图谱[81];(b)—SnO_2电极在不同pH环境下催化过程中的表面状态与法拉第效率之间的关系[81];(c)—SnO_2电极的原位XANES数据[50]。

(a)—in situ Raman spectrum of the surface composition evolution process of SnO_2 electrode; (b)—the relationship between the surface state and Faraday efficiency of SnO_2 electrodes in catalytic processes under different pH environments; (c)—in situ XANES data of SnO_2 electrode.

图7 Sn电极表面成分在CO_2RR过程中的演化过程[50,81]

Figure 7 Evolution of the surface composition of a Sn electrode during CO_2RR

部分还原SnO_2获得CO_2RR催化活性表面已经成为共识,但活性表面成分仍存在争议。Ning等[82]利用现场原位RS连续探测SnO_2催化剂在长时间CO_2RR过程中的拉曼峰变化,发现SnO_x的特征峰在加载−1.0 V(vs. RHE)偏压超过20 min后完全消失,但电极电势为−1.1 V的CO_2RR在9 h后仍然保持了80%以上的HCOOH法拉第效率。利用高分辨透射电子显微镜(High-resolution transmission electron microscope, HRTEM)和X射线衍射(X-ray diffraction, XRD)表征,发现金属Sn和SnO_2同时存在于反应后的催化剂中;通过离子剥离和X射线光电子谱(X-ray photoelectron spectroscopy, XPS)对元素分析,发现SnO_2存在于催化剂表层,而深层(深度约20 nm)以金属Sn为主。由此可知,SnO_2在CO_2RR过程中会形成SnO_2/Sn异质结,而该结构为反应的活性位点。尽管无法确认表层的SnO_2是否在转移样品时产生,但现场原位RS数据不支持长时间CO_2RR后仍有SnO_x存在的结论。关于表层SnO_2和内层Sn构成异质结的结论,仍缺乏原位实验数据支撑。Deng[83]利用ATR-

SEIRAS发现，Sn表面氢氧化物（Sn-OH）促进CO_2RR的新机制，即Sn-OH不直接与CO_2反应生成HCO_3*，而是促进H_2CO_3在附近生成，再被电化学还原生成$HCOO^-$。理论计算表明，适量的Sn-OH能实现最高效的CO_2RR，*OH表面覆盖率过高或过低都影响反应进程。Salvini等[77]的理论计算表明，SnO_2的（110）面对CO_2RR或HER没有活性，但SnO_2在负偏压下还原生成的金属Sn薄层对HCOOH具有极高的选择性。SnO_2在还原过程中，先失去表层的桥位氧原子（O_{br}），再失去面内氧原子（$O_{in\text{-}pl}$）。当形成双层Sn原子表面时，即获得较高的HCOOH选择性，具体表现为生成HCOOH所需的热力学势显著降低（见图8）。当SnO_2进一步还原为较厚的Sn原子壳层时，催化剂对HCOOH的选择性降低，而HER更具竞争力。目前，关于Sn基催化剂表层成分或异质结构仍然存在争论，金属Sn包覆SnO_x异质结或SnO_x包覆金属Sn异质结，都缺乏坚实的实验基础支撑，有待更高空间分辨能力和元素识别能力的原位观测技术在研究中发挥作用。

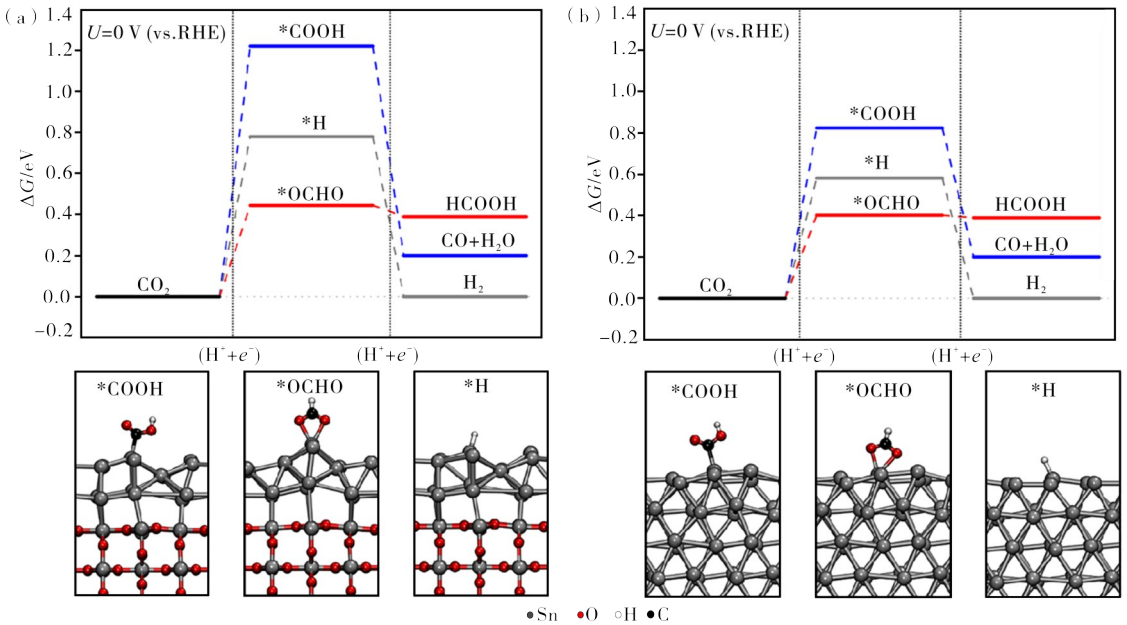

（a）—U= 0 V（vs. RHE）时2Sn@SnO_2表面对*COOH、*OCHO和*H的吸附能变化；（b）—U=0 V（vs. RHE）时Sn（101）表面对*COOH、*OCHO和*H的吸附能变化。

（a）—when U=0 V（vs. RHE），2Sn@SnO_2 the changes in adsorption energy of *COOH，*OCHO，and *H on the surface are shown；（b）—changes in adsorption energy of Sn（101）surface for *COOH，*OCHO，and *H at U= 0 V（vs. RHE）.

图8 CO_2RR在不同界面的反应路径图[77]

Figure 8 Reaction pathway depiction of CO_2RR at different interfaces

目前，部分学者仍不认同SnO_x是电催化CO_2RR产HCOOH的活性成分。He等[84]利用现场原位SERS研究了SnO_2和金属Sn催化剂在CO_2RR过程中的演化。结果表明，虽然两种催化剂在电还原过程中表现出不同的谱学特征，但在生成$HCOO^-$的选择性、分电流密度，以及Tafel斜率方面均表现出高度相似性。这是由于观察到的Sn^{4+}或Sn^{2+}氧化物并非催化活性物质，而金属Sn或其他无拉曼特征信号的Sn基氧化物才具有CO_2RR活性。

2.2 Bi基催化剂

金属Bi电极催化CO_2RR，首先由Komatsu等[85]于1995年提出。类似于Sn电极，Bi电极催化CO_2RR是有选择地产生HCOOH，并且在较负偏压下HCOOH的法拉第效率接近100%。然而，Bi基催化剂受到的关注远低于Sn基催化剂，这是因为其相对较少的储量和更高的价格。直到2013年，Dimeglio[86]和Medina-ramos[87]采用Bi电极催化离子液体中的CO_2RR产CO，使Bi基材料在CO_2RR研究中重新获得关注。金属Bi的化学稳定性较高，其Bi^{3+}/Bi的标准电极电势为0.308 V（vs. NHE）[88]。DFT计算表明，H原子在Bi（012）表面的吸附自由能（ΔG_H）为0.75 eV，高于典型的后过渡金属单质（如Au、Ag等）表面，意味着H原子较难被Bi金属吸附。与之相应，Bi金属是极不活跃的HER电极材料，位于HER火山图的底部位置[89]。因此，Bi基材料更适合在含水电解液内催化CO_2RR，通过有效抑制HER而实现更高的CO_2RR法拉第效率。确定Bi基催化剂的CO_2RR活性位点及反应机制，对高性能催化剂的开发和应用至关重要。

Sn基催化剂中的SnO_x在CO_2RR中的重要性早

已被广泛报道。同属于p区金属的Bi,在早期研究中也被假设其催化活性来源于氧化物(BiO_x)[90]。但是,因电催化CO_2RR施加电位远低于Bi^{3+}/Bi的标准电极电势,BiO_x不可避免地被还原为金属Bi。Bi基催化剂的活性位点和催化机理现阶段仍存在争议。Deng等[91]利用现场原位RS发现,虽然Bi_2O_3明显被还原为金属Bi,但仍有Bi—O结构对应的拉曼特征峰(127和314 cm^{-1})微弱存在。结合DFT计算,BiO_x的Bi—O结构可以加速CO_2的吸附和活化,同时将速率决定步骤从最初的电子转移过程,即形成CO_2^-*,转变为随后的质子化过程,即生成OCHO*。表明,BiO_x是电催化CO_2RR产HCOOH的活性成分。Li等[92]采用现场原位XAS观测二维Bi-MOF(金属有机框架,Metal-organic framework)催化剂在CO_2RR过程中结构的演变,发现Bi-MOF被部分还原,但仍有大量Bi^{3+}活性位点。原位表征技术揭示了较负电位仍有BiO_x残留,实验也同样肯定了大部分BiO_x在CO_2RR电位被还原为金属Bi,增加还原时间能显著减少BiO_x残留,但CO_2RR的法拉第效率相对稳定。结果表明,金属Bi才是真正的催化活性位点。Pander等[18]利用现场原位ATR-IRAS发现,BiO_x能被快速还原为金属Bi,而金属Bi的氧化过程却很缓慢且表现出半可逆性,在CO_2RR过程中BiO_x在较小偏压下被还原为金属Bi,而在后续的催化反应中保持稳定,并且未检测出Bi基碳酸盐的信号(见图9(a))。因此,将Bi基催化剂和铅(Pb)基催化剂一起归类为不依赖氧化物的CO_2RR催化剂。DFT计算表明[93],Bi—O键比Bi—C键具有更高的稳定性,则Bi表面吸附*OCHO相对于吸附*COOH更稳定,因而在CO_2RR过程中选择生成HCOOH而非CO。Dutta等[94]指出Bi_2O_3和金属Bi都有高HCOOH选择性,利用现场原位RS首次发现:在CO_2饱和的0.5 mol·L^{-1}的$KHCO_3$溶液中,Bi_2O_3表面出现了次碳酸铋(Bismuth subcarbonate,$(BiO)_2CO_3$),对应162 cm^{-1}的拉曼特征峰;随着电极电位下降,$(BiO)_2CO_3$与Bi_2O_3的特征峰强度均逐渐降低;在−0.8 V(vs. RHE)下,Bi_2O_3转变为金属Bi;$(BiO)_2CO_3$比Bi_2O_3更稳定,在−1.0 V才完全消失,表明其被完全还原为金属Bi(图9(b))。还原产生金属Bi与CO_2RR电流密度急剧增加同步发生,HCOOH的法拉第效率达到90%。当电极电势为−1.5V时,电流密度达到84.1 mA·cm^{-2},HCOOH的法拉第效率达到98%。因此,金属Bi是理想的CO_2RR产HCOOH的催化剂。

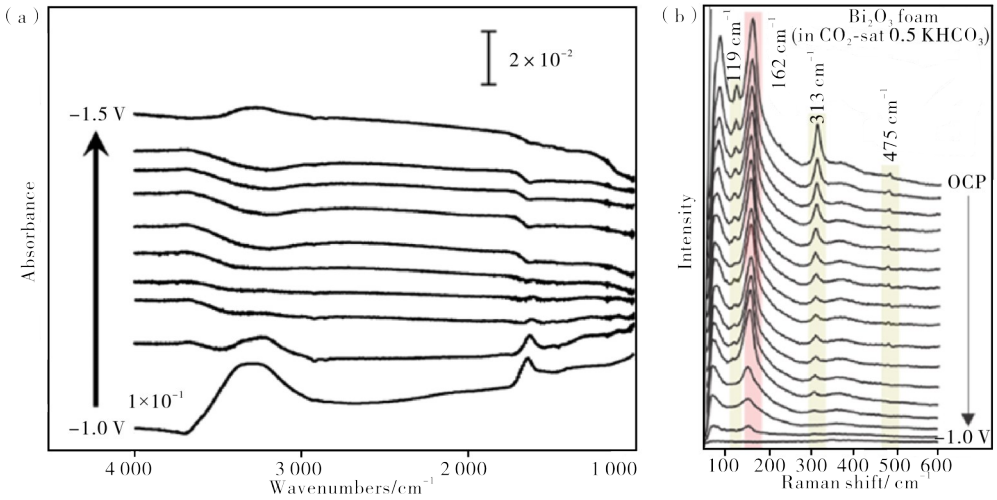

(a)—Bi薄膜电极在CO_2RR不同电位下的现场原位ATR-IRAS光谱(每个光谱相差50 mV电位)[18];
(b)—$(BiO)_2CO_3$/ Bi_2O_3复合催化剂在CO_2RR过程中的现场原位RS。
(a)—operando ATR-IRAS spectra of Bi thin film electrode at different CO_2RR potentials(with each spectrum differing by 50 mV potential); (b)—operando RS of $(BiO)_2CO_3/Bi_2O_3$ composite catalyst in CO_2RR process, sourced from reference.

图9 现场原位ATR-IRAS与现场原位Raman研究Bi基电极在CO_2RR过程中的演化[94]

Figure 9 Operando ATR-IRAS and operando Raman studies on the evolution of Bi based electrodes during CO_2RR process

2023年,Ren等[95]指出还原后的Cu_1Bi_1双金属催化剂具有丰富的Bi界面,相较于纯金属Bi,氧化物衍生的金属Bi对CO_2RR表现出更高的催化活性和HCOOH选择性。2024年,Zeng等[96]利用现场原位RS,揭示了Bi_2O_3多面体微晶在$KHCO_3$溶液中化学反应转化为$(BiO)_2CO_3$纳米片,然后在更负电位下衍生出金属Bi的完整过程(见图10),通过玻尔兹曼函数拟合拉曼峰强度变化可知,电位低于−0.56 V(vs. RHE)时,金属Bi为表面主要成分。这是由于Bi电极在低于−0.6 V电位下将CO_2转化为

$HCOO^-$，金属Bi为CO_2RR提供了活性位点，并且以$(BiO)_2CO_3$纳米片为中间态重构获得的金属Bi有更大比表面积，显著提升了反应的面电流密度。

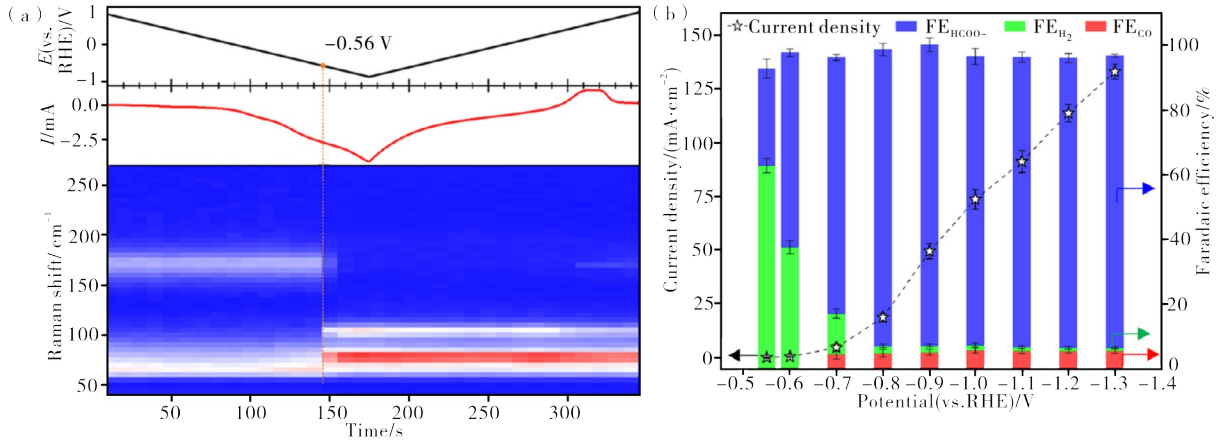

(a)—Bi-GDE在CO_2RR下电位相关的拉曼热图；(b)—Bi-GDE在CO_2RR不同电位下的电流密度和法拉第效率图。
(a)—potential dependent Raman thermogram of Bi GDE under CO_2RR; (b)—current density and Faraday efficiency of Bi GDE at different potentials of CO_2RR.

图10 Bi-GDE在CO_2RR下的拉曼热图及电流密度和法拉第效率图[96]

Figure 10 Heatmap of Raman spectra, current density, and Faraday efficiency of Bi-GDE catalyzed CO_2RR

金属Bi不同晶面的CO_2RR催化活性也是前沿课题。2023年，Yang等[97]使用现场原位RS、XRD和XAS技术研究了BiOX(X=Cl、Br、I)在电催化CO_2RR过程中的成分和晶格演化，结果发现：BiOX在还原电位下发生重构，逐渐生成金属Bi；卤化物X对还原产生金属Bi的暴露晶面有影响(见图11)，Br^-促进Bi(003)面的暴露，Cl^-促进Bi(012)晶面生长而抑制Bi(003)晶面，I^-催生了Bi(003)和Bi(012)的混合晶面；以BiOBr为前驱体产生的Bi(003)晶面有更高的CO_2RR催化活性和HCOOH选择性，能在−1.05 V获得148 mA·cm^{-2}的电流密度和91%的HCOOH法拉第效率，均优于相似电压下BiOCl还原产生的Bi(012)晶面，而BiOI还原产生的Bi金属表面催化CO_2RR的表现介于两者之间。

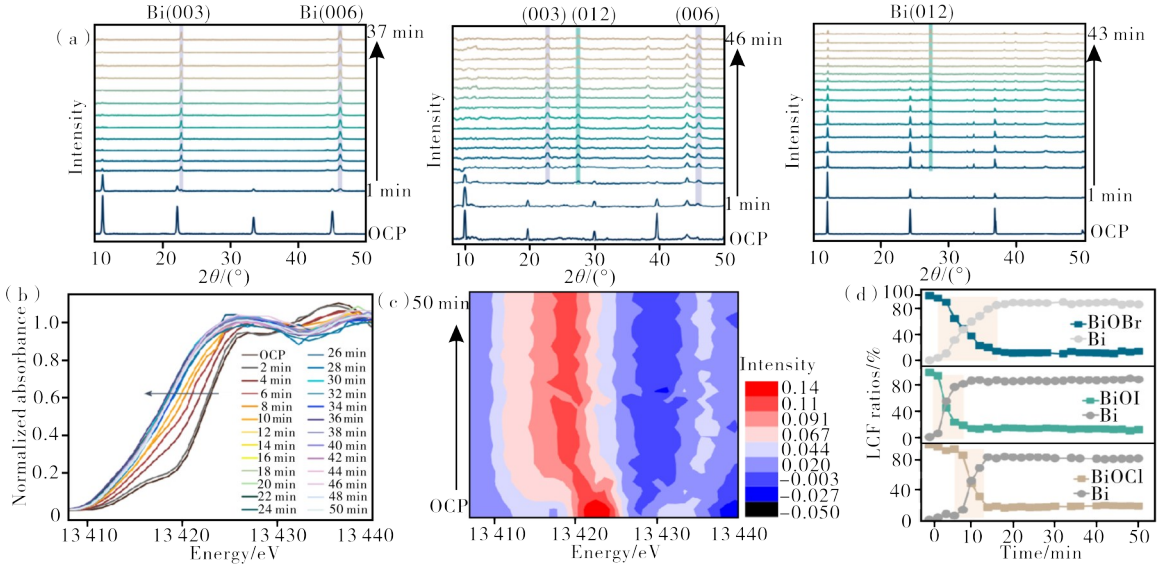

(a)—BiO_x与时间相关的原位XRD图；(b)—BiOBr随时间变化的原位XANES-BiL_3边缘图谱；(c)—BiOBr与原位XANES BiL_3边缘图谱相应的一阶导数热图；(d)—BiO_x与时间相关的XANES线性拟合结果。
(a)—in situ XRD pattern of BiO_x time-dependent at −1.15 V(vs. RHE) potential; (b)—in situ XANES-BiL_3 edge map of BiOBr over time; (c)—the first derivative heatmap corresponding to the edge spectra of BiOBr and in-situ XANES BiL_3; (d)—the linear fitting results of BiO_x and time-dependent XANES.

图11 在−1.15 V(vs. RHE)电位下的原位XRD图、原位XANES-BiL_3边缘图谱、一阶导数热图和XANES线性拟合图[97]

Figure 11 Time-dependent operando XRD pattern of BiO_x at −1.15 V(vs. RHE), and operando XANES-BiL_3 spectra, first derivative heatmap, linear fitting results

表明,平整的Bi(003)晶面比阶梯密度更高的Bi(012)晶面具有更高的CO_2RR催化活性,Bi晶体的平台位点具有催化活性。

大量原位表征技术支持Bi基催化剂表面在CO_2RR环境中会生成$(BiO_2)CO_3$[98],但部分学者仍对$(BiO_2)CO_3$的功能存在不同意见。An等[99]研究了花瓣状$(BiO_2)CO_3$纳米片催化CO_2RR产$HCOO^-$,并提出$(BiO_2)CO_3$通过稳定*OOCH中间体来提升催化活性。Liang等[100]利用现场原位SERS和ATR-IRAS观测,发现$BiPO_4$在电化学重构过程中,CO_3^{2-}与HCO_3^-的特征峰强度比值随时间推移而降低,支持重构过程形成了$Bi/(BiO_2)CO_3$界面,导致局部CO_3^{2-}浓度降低。结合DFT计算,发现Bi原子在$Bi/(BiO_2)CO_3$界面上的电荷再分布导致反应中间体吸附行为改变,进而影响了CO_2的活化和还原。金属Bi在CO_2RR过程中的表面成分、中间产物、电子态等关键信息,仍有待实验和理论进一步阐明。

2.3 In基催化剂

In电极的CO_2RR催化效果与Sn电极相似。Hori等[14]指出,In电极在-1.55V(vs. SHE)电压下,可以达到5 mA·cm^{-2}的电流密度,以及94.9%的HCOOH法拉第效率。在相同条件下,In电极的法拉第效率甚至比Sn电极(88.4%)更高。与Sn的研究进程类似,科学界开始使用原位观测技术去解析In的催化活性位点,并试图提高其催化活性。

2014年,Detweiler等[101]通过对比实验和原位表征技术,证明了In电极对$HCOO^-$的高催化效率很大程度上取决于表面状态。被腐蚀掉氧化层的In电极催化效率较低,而阳极氧化获得较厚氧化层的In电极对$HCOO^-$选择性更高。利用现场原位ATR-IRAS,确定了氧化铟(Indium oxide, In_2O_3)在CO_2RR过程中与水反应形成氢氧化铟(Indium hydroxide, $In(OH)_3$),$In(OH)_3$与溶解CO_2反应形成$In\text{-}CO_3$,并将CO_2限制在催化剂表面,在后续还原步骤中又将CO_2还原生成$HCOO^-$。Ma等[102]开发了一种从过氧化氢铟(Indium oxyhydroxide, InOOH)纳米片原位生成的In基催化剂。在循环伏安测试中,利用同步辐射X射线进行XRD实验(见图12),观察到InOOH纳米片在CO_2RR中动态生成金属In,但仍保留部分InOOH,表明循环伏安过程中形成的In催化位点具有更高活性。现场原位RS

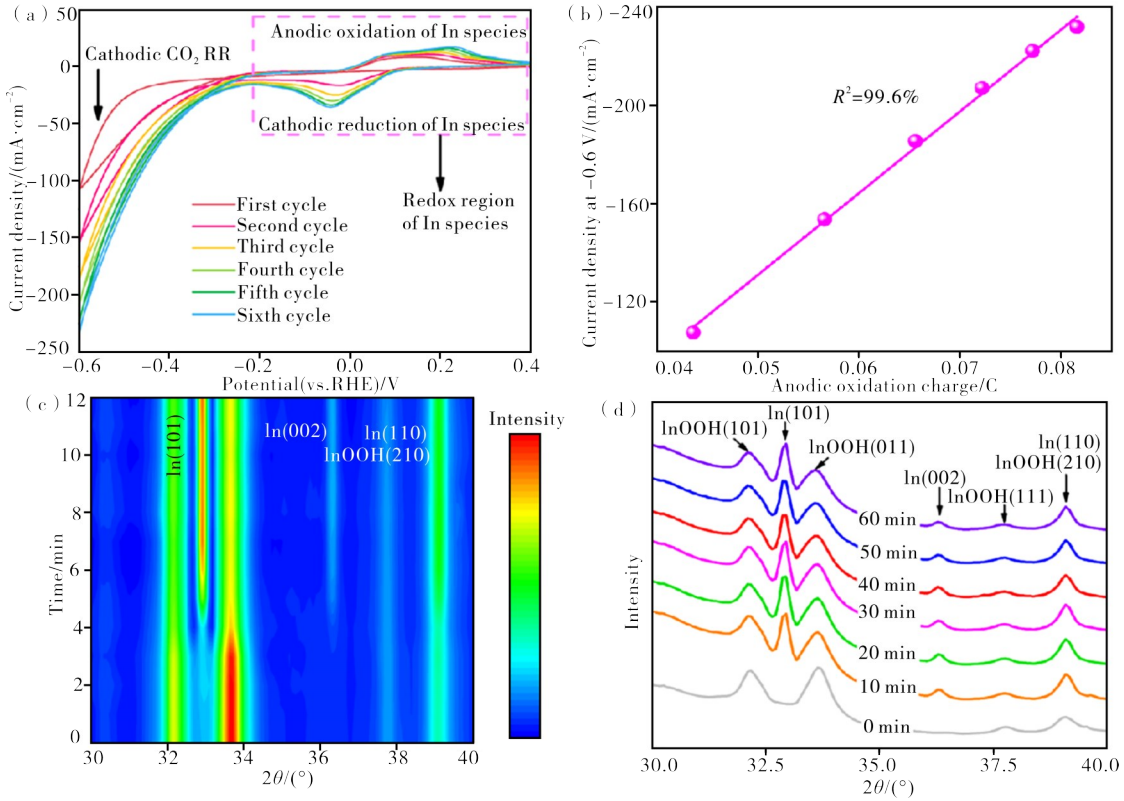

(a)—InOOH纳米片的循环伏安曲线;(b)—CO_2RR的催化活性与In氧化还原峰的面积拟合数据;(c、d)—原位XRD热图与波纹图。

(a)—cyclic voltammetry curve of InOOH nanosheets; (b)—fit data between the catalytic activity of CO_2RR and the area of the In redox peak; (c,d)—in situ XRD thermogram and ripple pattern.

图12 InOOH纳米片原位生成的In基催化剂的性能[102]

Figure 12 Performance of In-based catalysts generated in situ from InOOH nanosheets

也表征了In基催化剂的活性变化。在−0.4 V(vs. RHE)时，*COO^-和*$HCOO^-$的拉曼信号随时间逐渐增强，表明金属In生成对CO和HCOOH的催化活性都有提升；随施加电位向更负移动，*COO^-的吸附减弱，说明CO的生成被抑制，催化剂对HCOOH有更高选择性。

2.4 Pb基催化剂

Pb基催化剂因毒性而较少获得应用研究，已报道的工作主要是反应机理相关的基础研究。CO_2RR在Pb电极表面的过电位高于其他p区金属电极，但HCOOH的法拉第效率并无劣势[103]。Back等[104]采用DFT对Pb催化CO_2RR的反应机理进行了分析，认为Pb电极有很强的O*亲和性，而对H*和C*的亲和性较弱，表明Pb基催化剂具有HCOOH选择性。Zhao等[105]认为Pb在不同的溶液和气氛环境中具有不同的吸附选择性，CO_2在Pb表面可通过HCOO*和*COOH两种中间体路径产生HCOOH。Pander等[18]通过现场原位ATR-IRAS发现，Pb电极表面没有形成Pb-CO_3，CO_2RR的路径可能是*CO_2→*COOH→COOH，而不以HCOO*为中间体。同时，Pb电极经阳极氧化处理后，HCOOH的法拉第效率提升，表明表面氧化物有助于提升CO_2RR性能。Lee等[106]认为阳极经氧化处理后能提升Pb电极抑制竞争性HER，而不提升CO_2RR活性。

3 合金化

金属单质催化剂的表面电子结构相对确定，即使晶格应力、晶面取向、晶体结构等因素会影响其电子结构，进而影响反应中间产物的吸附能及反应动力学[107]。然而，金属单质的催化性能可调节幅度较小，催化效率和选择性无法有显著提升。在更大范围内合理优化催化剂的表面电子结构，有望提高催化剂的活性、选择性及稳定性[108-110]。合金化是将主体金属与其他金属或非金属元素按照一定比例混合，并形成均匀的固溶体。合金化能显著调整催化剂的电子结构，优化中间产物的吸附能，并抑制竞争反应，该策略已被广泛应用于高性能催化剂的开发[111-116]。

Sn的原子半径与电子结构，决定了其能与多种金属形成合金，被誉为“金属胶水”[117]。多种Sn基双金属或三金合金被报道用于电催化CO_2RR，如Sn-Cu[118]、Sn-Bi[119]、Sn-Cu-Zn[120]等。Cu相较于Sn有更强的CO_2吸附能力，且能形成*COOH和*CO中间产物，与Sn表面吸附*OCOH中间产物有显著差异[121]。因此，Cu-Sn合金有助于CO_2吸附，并有望降低反应活化能而提高反应效率。Wang等[122]通过电沉积和煅烧工艺制备了异质结构的Cu-Sn合金(Cu_3Sn/Cu_6Sn_5)催化剂，并将其支撑在多孔铜泡沫上，其在气体扩散电极中展现出高达148 mA·cm^{-2}的电流密度。DFT计算结果表明，异质结构的Cu_3Sn/Cu_6Sn_5催化剂不仅抑制了析氢反应，而且有利于甲酸的生成。但是，Cu-Sn合金的CO_2RR催化选择性对成分极为敏感。当微量Sn掺杂Cu时，无论电极浸润在电解液中还是以气体扩散电极形式工作，都选择性生成CO[123-124]；而Sn元素含量高于23.5 μmol·cm^{-2}时，反应产物以HCOOH为主[125]。究其原因，不排除Cu-Sn去合金化造成的Sn表面富集现象。Cu-Sn合金催化剂的活性成分和催化机制仍存在争议。

Sn-Bi合金能通过抑制H_2和CO的形成来促进甲酸盐的生成。Ren等[114]合成出纳米褶皱诱导的Sn-Bi双金属催化剂，使甲酸盐的局部电流密度达140 mA·cm^{-2}，且160 h内可在宽电压窗口下保持较高的法拉第效率(大于90%)。通过DFT计算，对比了体相有序合金(如Sn-Bi合金)与表面合金(如Sn-Bi双金属界面)的差异，发现与Sn-Bi合金和纯Sn相比，Sn-Bi界面提供了最佳的p带中心上移，使价电子适度耗尽，导致竞争吸附COOH的Sn-C杂化减弱，并使得吸附HCOO的Sn-O杂化增强，由此提供了更高的甲酸盐选择性。此外，现场原位EXAFS被用于验证Sn-Bi的电子密度转移，这影响了材料的电子结构和催化活性。现场原位RS则被用于检测不同电位下吸附在Sn-Bi双金属界面上的中间体。

除了Sn基合金外，其他许多金属也被用于合成合金以提高催化效率。Cao等[49]制备了原子级Bi掺杂的In基催化剂(Bi-In/C)，实现了高达95.1%的$HCOO^-$法拉第效率，在测试电位范围内展示了9 d的长期稳定性；Yao等[126]研发了原子级In掺杂的Cu基催化剂($Cu_{100}In_x$-CP)，在−1.2 V(vs. RHE)电位下实现了85.11%的C_{2+}产品法拉第效率，并且部分电流密度达到了36.3 mA·cm^{-2}；Cui等[127]合成了碲(Te)掺杂的Bi纳米颗粒，负载在超薄氮(N)掺杂碳纳米片(N-CNSs)上，在−0.8—−1.2 V(vs. RHE)的电位窗口内有高于90%的$HCOO^-$法拉第效率，且在−1.2 V(vs. RHE)时产$HCOO^-$的电流密度达到130 mA·cm^{-2}。

综上所述，p区金属通过合金化策略，优化了中间产物的吸附能、抑制了竞争反应、提升了催化剂稳

定性,是开发高性能催化剂的可行路径,有望推动CO_2RR产HCOOH的工业化进程。合金催化剂在CO_2RR中的成分和结构演化、中间产物吸附状态、反应路径和动力学等基础问题,都迫切需要原位分析技术辅助寻找答案。

4 总结与展望

电催化CO_2RR产HCOOH具有潜在的经济价值,是实现"碳闭环"的可行关键技术。p区金属(如Sn、Bi、In、和Pb)能以高法拉第效率催化CO_2RR产HCOOH,解析其反应机理有助于改良、设计新型催化剂。原位观测技术帮助识别电化学状态下催化剂的表面活性位点,甚至催化中间产物,推动反应机理认知。现有技术聚焦催化界面的化学成键、物质成分和结构、近表面产物等,与DFT等理论计算相结合,能描绘出催化过程,在催化领域已经得到广泛的使用。然而,原位观测技术仍有局限性,如催化反应受催化剂表面若干原子层的调控,且反应进程受到界面环境影响。基于光吸收或非线性散射的表面表征技术提供更多体态信息,干扰表面态分析和判断。实验观测催化中间产物仍然极具挑战,而且至今尚缺乏近表面反应物和产物浓度分析方法。虽然表面分析方法均提供了反应稳态下的统计结果,但无法提供反应瞬态信息。

针对以上问题,原位观测技术需在时空分辨能力继续提升。例如引入超快分析方法,获取化学成键、声子传导、结构演化的即时信息。或采用表面更敏感的相互作用方式来表征电催化界面的物质信息,如借助SERS、TERS等获取反应中间产物信息。先进原位观测技术旨在探究催化活性物质及其反应机理,为开发实用型催化剂和优化反应环境提供重要基础支撑。

参考文献:

[1] HARRIS P G. Global ethics and climate change global climate change[M]. Edinburgh: Edinburgh University, 2016: 17-28.

[2] VOGT C, MONAI M, KRAMER G J, et al. The renaissance of the Sabatier reaction and its applications on earth and in space [J]. Nature Catalysis, 2019, 2(3): 188-197.

[3] HEPBURN C, ADLEN E, BEDDINGTON J, et al. The technological and economic prospects for CO_2 utilization and removal [J]. Nature, 2019, 575(7781): 87-97.

[4] MIKKELSEN M, JØRGENSEN M, KREBS F C. The teraton challenge: A review of fixation and transformation of carbon dioxide [J]. Energy Environ Sci, 2010, 3(1): 43-81.

[5] 李双成, 王巧玲, 刘迎陆."双碳"目标下的中国可再生能源发展:机遇与挑战[J]. 气候与环境研究, 2024, 29(3): 390-8.

[6] 卢冠初, WANG Z, BHATTI U, 等. 二氧化碳捕获技术的最新进展:综述[J]. 清洁能源科学与技术, 2023(1):1-42.

[7] ÓBRIEN C P, MIAO R K, SHAYESTEH ZERAATI A, et al. CO_2 electrolyzers [J]. Chemical Reviews, 2024, 124(7): 3648-3693.

[8] DE LUNA P, HAHN C, HIGGINS D, et al. What would it take for renewably powered electrosynthesis to displace petrochemical processes? [J/OL]. Science, 2019, 364: 6438. https://www. science. org/doi/10.1126/science.aav3506.

[9] PETER S C. Reduction of CO_2 to chemicals and fuels: A solution to global warming and energy crisis [J]. ACS Energy Letters, 2018, 3(7): 1557-1561.

[10] LONG C, LI X, GUO J, et al. Electrochemical reduction of CO_2 over heterogeneous catalysts in aqueous solution: recent progress and perspectives [J]. Small Methods, 2018, 3(3): 1800369.

[11] QIAO J, LIU Y, HONG F, et al. A review of catalysts for the electroreduction of carbon dioxide to produce low-carbon fuels [J]. Chem Soc Rev, 2014, 43(2): 631-675.

[12] WELCH A J, DUCHENE J S, TAGLIABUE G, et al. Nanoporous gold as a highly selective and active carbon dioxide reduction catalyst [J]. ACS Applied Energy Materials, 2019, 2(1): 164-170.

[13] KIM B, MA S, MOLLY JHONG H R, et al. Influence of dilute feed and pH on electrochemical reduction of CO2 to CO on Ag in a continuous flow electrolyzer [J]. Electrochimica Acta, 2015, 166: 271-276.

[14] HORI Y, WAKEBE H, TSUKAMOTO T, et al. Electrocatalytic process of CO selectivity in electrochemical reduction of CO_2 at metal electrodes in aqueous media [J]. Electrochimica Acta, 1994, 39(11): 1833-1839.

[15] DU S, YANG P, LI M, et al. Catalysts and electrolyzers for the electrochemical CO_2 reduction reaction: From laboratory to industrial applications [J]. Chem Commun, 2024, 60(10): 1207-1221.

[16] KORTLEVER R, SHEN J, SCHOUTEN K J, et al. Catalysts and reaction pathways for the electrochemical reduction of carbon dioxide [J]. J Phys Chem Lett, 2015, 6(20): 4073-4082.

[17] KIBRIA M G, EDWARDS J P, GABARDO C M,

et al. Electrochemical CO_2 reduction into chemical feedstocks: From mechanistic electrocatalysis models to system design [J]. Adv Mater, 2019, 31(31): e1807166.

[18] PANDER J E, BARUCH M F, BOCARSLY A B. Probing the mechanism of aqueous CO_2 reduction on post-transition-metal electrodes using ATR-IR spectroelectrochemistry [J]. ACS Catalysis, 2016, 6(11): 7824-7833.

[19] JIN S, HAO Z, ZHANG K, et al. Advances and challenges for the electrochemical reduction of CO_2 to CO: From fundamentals to industrialization [J]. Angew Chem Int Ed Engl, 2021, 60(38): 20627-20648.

[20] SONG X, XU L, SUN X, et al. In situ/operando characterization techniques for electrochemical CO_2 reduction [J]. Science China Chemistry, 2023, 66(2): 315-323.

[21] ZOU Y, WANG S. An investigation of active sites for electrochemical CO_2 reduction reactions: From in situ characterization to rational design [J]. Adv Sci (Weinh), 2021, 8(9): 2003579.

[22] CHEN Z, WANG X, MILLS J P, et al. Two-dimensional materials for electrochemical CO_2 reduction: Materials, in situ/operando characterizations, and perspective [J]. Nanoscale, 2021, 13(47): 19712-19739.

[23] LONG L, JU W, YANG H Y, et al. Dimensional design for surface-enhanced raman spectroscopy [J]. ACS Mater Au, 2022, 2(5): 552-75.

[24] HEIDARY N, LY K H, KORNIENKO N. Probing CO_2 conversion chemistry on nanostructured surfaces with operando vibrational spectroscopy [J]. Nano Lett, 2019, 19(8): 4817-26.

[25] 杨金梅, 张海明, 王旭, 等. 红外光谱和拉曼光谱的联系和区别[J]. 物理与工程, 2014, 24(4): 26-29.

[26] REN B, LI X Q, SHE C X, et al. Surface Raman spectroscopy as a versatile technique to study methanol oxidation on rough Pt electrodes [J]. Electrochimica Acta, 2000, 46(2): 193-205.

[27] CHEN J, MA B, XIE Z, et al. Bifunctional porous SnO_2/Ag nanofibers for efficient electroreduction of carbon dioxide to formate and its mechanism elucidation by in-situ surface-enhanced Raman scattering [J]. Applied Catalysis B: Environmental, 2023, 325:122350.

[28] YEO B S, KLAUS S L, ROSS P N, et al. Identification of hydroperoxy species as reaction intermediates in the electrochemical evolution of oxygen on gold [J]. Chemphyschem, 2010, 11(9): 1854-1857.

[29] YEO B S, BELL A T. Enhanced activity of gold-supported cobalt oxide for the electrochemical evolution of oxygen [J]. Journal of the American Chemical Society, 2011, 133(14): 5587-5593.

[30] YEO B S, BELL A T. In situ raman study of nickel oxide and gold-supported nickel oxide catalysts for the electrochemical evolution of oxygen [J]. The Journal of Physical Chemistry C, 2012, 116(15): 8394-8400.

[31] ZENG Z C, HU S, HUANG S C, et al. Novel electrochemical raman spectroscopy enabled by water immersion objective [J]. Anal Chem, 2016, 88(19): 9381-9385.

[32] LI J F, ZHANG Y J, DING S Y, et al. Core-shell nanoparticle-enhanced raman spectroscopy [J/OL]. Chemical Reviews, 2017, 117(7): 5002-5069. https://pubs. acs. org/doi/10.1021/acs. chemrev. 6b00596.

[33] LIN X D, LI J F, HUANG Y F, et al. Shell-isolated nanoparticle-enhanced Raman spectroscopy: Nanoparticle synthesis, characterization and applications in electrochemistry [J/OL]. Journal of Electroanalytical Chemistry, 2013, 688:5-11. https://linkinghub. elsevier. com/retrieve/pii/S1572665712002718.

[34] NIE S, EMORY S R. Probing single molecules and single nanoparticles by surface-enhanced Raman scattering [J]. Science, 1997, 275(5303): 1102-1106.

[35] TAFAZOLI S, YUSUFOĞLU M, BALKAN T, et al. In-situ surface enhanced Raman spectroscopy investigations on surface transformations of oxide derived copper electrodes during CO_2RR [J]. Journal of Catalysis, 2023, 423:118:128.

[36] LIU H, QI Z, SONG L. In situ electrocatalytic infrared spectroscopy for dynamic reactions [J]. The Journal of Physical Chemistry C, 2021, 125(44): 24289-24300.

[37] MOSS D, NABEDRYK E, BRETON J, et al. Redox-linked conformational changes in proteins detected by a combination of infrared spectroscopy and protein electrochemistry: Evaluation of the technique with cytochrome C [J]. Eur J Biochem, 1990, 187(3): 565-572.

[38] KATO Y, NOGUCHI T. Long-range interaction between the Mn_4CaO_5 cluster and the non-heme iron center in photosystem ii as revealed by FTIR spectroelectrochemistry [J]. Biochemistry, 2014, 53(30): 4914-4923.

[39] TUTUNEA F, RYAN M D. Visible and infrared spectroelectrochemistry of cobalt porphinones and

porphinediones [J]. Journal of Electroanalytical Chemistry, 2012, 670:16-22.
[40] DAI Y, PROSHLYAKOV D A, ZAK J K, et al. Optically transparent diamond electrode for use in IR transmission spectroelectrochemical measurements [J]. Analytical Chemistry, 2007, 79(19): 7526-7533.
[41] ALWIS L K H K, MUCALO M R, INGHAM B. Anodically polarized nickel electrodes in DMSO or DMF solutions of pseudohalide ions: IR spectroelectrochemical studies [J]. Journal of the Electrochemical Society, 2013, 160(11): H803-H812.
[42] LIU L, ZENG L, WU L, et al. Label-free surface-enhanced infrared spectroelectrochemistry studies the interaction of cytochrome C with cardiolipin-containing membranes [J]. The Journal of Physical Chemistry C, 2015, 119(8): 3990-3999.
[43] HANDOKO A D, WEI F, JENNDY, et al. Understanding heterogeneous electrocatalytic carbon dioxide reduction through operando techniques [J]. Nature Catalysis, 2018, 1(12): 922-934.
[44] WAIN A J, ÓCONNELL M A. Advances in surface-enhanced vibrational spectroscopy at electrochemical interfaces [J]. Advances in Physics: X, 2017, 2(1): 188-209.
[45] GLASSFORD S E, BYRNE B, KAZARIAN S G. Recent applications of ATR FTIR spectroscopy and imaging to proteins [J]. Biochim Biophys Acta, 2013, 1834(12): 2849-2858.
[46] KRETSCHMANN E. Die bestimmung optischer konstanten von metallen durch anregung von oberflächenplasmaschwingungen [J]. Zeitschrift Für Physik A Hadrons and Nuclei, 1971, 241 (4): 313-324.
[47] BARUCH M F, PANDER J E, WHITE J L, et al. Mechanistic insights into the reduction of CO_2 on tin electrodes using in situ ATR-IR spectroscopy [J/OL]. ACS Catalysis, 2015, 5(5): 3148-3156. https://pubs.acs.org/doi/10.1021/acscatal.5b00402.
[48] BARUCH M F, PANDER J E, WHITE J L, et al. Mechanistic insights into the reduction of CO_2 on tin electrodes using in situ ATR-IR spectroscopy [J]. ACS Catalysis, 2015, 5(5): 3148-3156.
[49] CAO X, WULAN B, WANG Y, et al. Atomic bismuth induced ensemble sites with indium towards highly efficient and stable electrocatalytic reduction of carbon dioxide [J]. Sci Bull (Beijing), 2023, 68(10): 1008-1016.
[50] DUTTA A, KUZUME A, KALIGINEDI V, et al. Probing the chemical state of tin oxide NP catalysts during CO_2 electroreduction: A complementary operando approach [J]. Nano Energy, 2018, 53: 828-840.
[51] WU Z, WU H, CAI W, et al. Engineering bismuth-tin interface in bimetallic aerogel with a 3D porous structure for highly selective electrocatalytic CO_2 reduction to HCOOH [J]. Angew Chem Int Ed Engl, 2021, 60(22): 12554-12559.
[52] XIAO L, LIU X, ZHOU R, et al. Facile synthesis of high-performance indium nanocrystals for selective CO_2-to-formate electroreduction [J]. Energy Conversion and Management, 2021, 231: 113847.
[53] TIMOSHENKO J, ROLDAN CUENYA B. In Situ/operando electrocatalyst characterization by X-ray absorption spectroscopy [J]. Chem Rev, 2021, 121 (2): 882-961.
[54] YANG Y, WANG Y, XIONG Y, et al. In situ X-ray absorption spectroscopy of a synergistic Co-Mn oxide catalyst for the oxygen reduction reaction [J]. J Am Chem Soc, 2019, 141(4): 1463-1466.
[55] CHANG C J, ZHU Y, WANG J, et al. In situ X-ray diffraction and X-ray absorption spectroscopy of electrocatalysts for energy conversion reactions [J]. Journal of Materials Chemistry A, 2020, 8 (37): 19079-19112.
[56] BENFATTO M, MENEGHINI C. A close look into the low energy region of the XAS spectra: The XANES region [M]. Heidelberg: Springer Berlin Heidelberg, 2015: 213-240.
[57] TSAPATSARIS N, BEESLEY A M, WEIHER N, et al. High throughput in situ XAFS screening of catalysts [M]. AIP Publishing: AIP Conference Proceedings, 2007: 597-599.
[58] BORDIGA S, GROPPO E, AGOSTINI G, et al. Reactivity of surface species in heterogeneous catalysts probed by in situ X-ray absorption techniques [J]. Chemical Reviews, 2013, 113(3): 1736-1850.
[59] WENG Z, WU Y, WANG M, et al. Active sites of copper-complex catalytic materials for electrochemical carbon dioxide reduction [J]. Nat Commun, 2018, 9 (1): 415.
[60] MISTRY H, VARELA A S, BONIFACIO C S, et al. Highly selective plasma-activated copper catalysts for carbon dioxide reduction to ethylene [J]. Nat Commun, 2016, 7:12123.
[61] HE F, CHEN W, CHEN J Q, et al. The effect of water on the quantification of volatile species by differential electrochemical mass spectrometry [J]. Anal Chem, 2021, 93(13): 5547-5555.
[62] MORA-HERNANDEZ J M, GONZÁLEZ-SUáREZ W I, MANZO-ROBLEDO A, et al. A comparative

differential electrochemical mass spectrometry (DEMS) study towards the CO_2 reduction on Pd, Cu, and Sn -based electrocatalyst [J]. Journal of CO_2 Utilization, 2021, 47: 101504.

[63] SANTIAGO-RAMíREZ C R, VERA-ITURRIAGA J, DEL ANGEL P, et al. DEMS and RAMAN study of the monatomic hydrogen adsorption during electro-reduction of NO_3- and NO2- at Pt nanoparticles supported at W18O49-ZrO_2-C nanocomposite [J/OL]. Applied Catalysis B: Environmental, 2021, 282: 119545. https://linkinghub.elsevier.com/retrieve/pii/S0926337320309607.

[64] WANG X, KLINGAN K, KLINGENHOF M, et al. Morphology and mechanism of highly selective Cu(II) oxide nanosheet catalysts for carbon dioxide electroreduction [J]. Nat Commun, 2021, 12(1): 794.

[65] BALTRUSCHAT H. Differential electrochemical mass spectrometry [J]. J Am Soc Mass Spectrom, 2004, 15(12): 1693-1706.

[66] ABD-EL-LATIF A A, BONDUE C J, ERNST S, et al. Insights into electrochemical reactions by differential electrochemical mass spectrometry [J]. TrAC Trends in Analytical Chemistry, 2015, 70:4-13.

[67] ZHAO K, JIANG X, WU X, et al. Recent development and applications of differential electrochemical mass spectrometry in emerging energy conversion and storage solutions [J]. Chem Soc Rev, 2024, 53(13): 6917-6959.

[68] FEASTER J T, SHI C, CAVE E R, et al. Understanding selectivity for the electrochemical reduction of carbon dioxide to formic acid and carbon monoxide on metal electrodes [J/OL]. ACS Catalysis, 2017, 7(7): 4822-4827. https://pubs.acs.org/doi/10.1021/acscatal.7b00687.

[69] CHENG F, ZHANG X, MU K, et al. Recent progress of Sn-based derivative catalysts for electrochemical reduction of CO_2 [J]. Energy Technology, 2020, 9(1): 2000799.

[70] CHENG W, XU X, LIAO Q, et al. In situ dynamic re-structuring and interfacial evolution of SnS_2 for high-performance electrochemical CO_2 reduction to formate [J]. Chemical Engineering Journal, 2024, 480: 147922.

[71] DENG Y, ZHAO J, WANG S, et al. Operando spectroscopic analysis of axial oxygen-coordinated single-sn-atom sites for electrochemical CO_2 reduction [J]. Journal of the American Chemical Society, 2023, 145(13): 7242-7251.

[72] BARUCH M F, PANDER J E, WHITE J L, et al. Mechanistic insights into the reduction of CO_2 on tin electrodes using in situ ATR-IR spectroscopy [J]. ACS Catalysis, 2015, 5(5): 3148-3156.

[73] CHEN Y, KANAN M W. Tin oxide dependence of the CO_2 reduction efficiency on tin electrodes and enhanced activity for tin/tin oxide thin-film catalysts [J/OL]. Journal of the American Chemical Society, 2012, 134(4): 1986-1989 . https://pubs.acs.org/doi/10.021/ja2108799.

[74] DUTTA A, KUZUME A, RAHAMAN M, et al. Monitoring the chemical state of catalysts for CO_2 electroreduction: An in operando study [J/OL]. ACS Catalysis, 2015, 5(12): 7498-7502. https://pubs.acs.org/doi/10.1021/acscatal.5b02322.

[75] JING H, ZHAO P, LIU C, et al. Surface-enhanced raman spectroscopy for boosting electrochemical CO_2 reduction on amorphous-surfaced tin oxide supported by MXene [J]. ACS Appl Mater Interfaces, 2023, 15(51): 59524-59533.

[76] NING S, WANG J, XIANG D, et al. Electrochemical reduction of SnO_2 to Sn from the bottom: In-situ formation of SnO_2/Sn heterostructure for highly efficient electrochemical reduction of carbon dioxide to formate [J/OL]. Journal of Catalysis, 2021, 399: 67-74. https://linkinghub.elsevier.com/retrieve/pii/S0021951721001809.

[77] SALVINI C, RE FIORENTIN M, RISPLENDI F, et al. Active surface structure of SnO_2 catalysts for CO_2 reduction revealed by ab initio simulations [J/OL]. The Journal of Physical Chemistry C, 2022, 126(34): 14441-14447. https://creativecommons.org/licenses/by/4.0/.

[78] POURBAIX M, BURBANK J. Atlas D-equilibres electrochimiques [J]. Journal of the Electrochemical Society, 1964, 111(1): 14C.

[79] LEE S, OCON J D, SON Y I, et al. Alkaline CO_2 electrolysis toward selective and continuous HCOO− production over SnO_2 nanocatalysts [J]. The Journal of Physical Chemistry C, 2015, 119(9): 4884-4890.

[80] CHEN Y, KANAN M W. Tin oxide dependence of the CO_2 reduction efficiency on tin electrodes and enhanced activity for tin/tin oxide thin-film catalysts [J]. J Am Chem Soc, 2012, 134(4): 1986-1989.

[81] DUTTA A, KUZUME A, RAHAMAN M, et al. Monitoring the chemical state of catalysts for CO_2 electroreduction: An in operando study [J]. ACS Catalysis, 2015, 5(12): 7498-7502.

[82] NING S, WANG J, XIANG D, et al. Electrochemical reduction of SnO_2 to Sn from the bottom: In-situ formation of SnO_2/Sn heterostructure for highly efficient electrochemical reduction of carbon

dioxide to formate [J]. Journal of Catalysis, 2021, 399:67-74.
[83] DENG W, ZHANG L, LI L, et al. Crucial role of surface hydroxyls on the activity and stability in electrochemical CO_2 reduction [J]. J Am Chem Soc, 2019, 141(7): 2911-2915.
[84] HE M, XU B, LU Q. Probing the role of surface speciation of tin oxide and tin catalysts on CO_2 electroreduction combining in situ Raman spectroscopy and reactivity investigations [J]. Chinese Journal of Catalysis, 2022, 43(6): 1473-1477.
[85] KOMATSU S, YANAGIHARA T, HIRAGA Y, et al. Electrochemical reduction of CO_2 at Sb and Bi Electrodes in $KHCO_3$ solution [J]. Denki Kagaku oyobi Kogyo Butsuri Kagaku, 1995, 63(3): 217-224.
[86] DIMEGLIO J L, ROSENTHAL J. Selective conversion of CO_2 to CO with high efficiency using an inexpensive bismuth-based electrocatalyst [J]. Journal of the American Chemical Society, 2013, 135(24): 8798-8801.
[87] MEDINA-RAMOS J, DIMEGLIO J L, ROSENTHAL J. Efficient reduction of CO_2 to CO with high current density using in situ or EX situ prepared bi-based materials [J]. Journal of the American Chemical Society, 2014, 136(23): 8361-8367.
[88] HAYNES W M. Handbook of chemistry and physics [M]. CRC Press: Boca Raton, 2016.
[89] GREELEY J, JARAMILLO T F, BONDE J, et al. Computational high-throughput screening of electrocatalytic materials for hydrogen evolution [J]. Nature Materials, 2006, 5(11): 909-913.
[90] YANG Z, OROPEZA F E, ZHANG K H L. P-block metal-based (Sn, In, Bi, Pb) electrocatalysts for selective reduction of CO_2 to formate [J/OL]. APL Materials, 2020, 8(6): 60901. https://pubs.aip.org/apm/article/8/6//1062388/P-block-metal-based-Sn-In-Bi-Pb-electrocatalysts.
[91] DENG P, WANG H, QI R, et al. Bismuth oxides with enhanced bismuth-oxygen structure for efficient electrochemical reduction of carbon dioxide to formate [J]. ACS Catalysis, 2020, 10(1): 743-750.
[92] LI F, GU G H, CHOI C, et al. Highly stable two-dimensional bismuth metal-organic frameworks for efficient electrochemical reduction of CO_2 [J]. Applied Catalysis B: Environmental, 2020, 277:119241.
[93] WALKER R J, POUGIN A, OROPEZA F E, et al. Surface termination and CO_2 adsorption onto bismuth pyrochlore oxides [J]. Chemistry of Materials, 2016, 28(1): 90-96.
[94] DUTTA A, ZELOCUALTECATL MONTIEL I, KIRAN K, et al. A tandem (Bi_2O_3→Bimet) catalyst for highly efficient ec-CO_2 conversion into formate: Operando raman spectroscopic evidence for a reaction pathway change [J]. ACS Catalysis, 2021, 11(9): 4988-5003.
[95] REN H, WANG X, ZHOU X, et al. In-situ constructing Cu1Bi1 bimetallic catalyst to promote the electroreduction of CO_2 to formate by synergistic electronic and geometric effects [J]. Journal of Energy Chemistry, 2023, 79:263-271.
[96] ZENG J, MONTI N B D, CHEN T, et al. Evolution of bismuth electrodes activating electrosynthesis of formate from carbon dioxide reduction [J]. Catalysis Today, 2024, 437:114743.
[97] YANG S, AN H, ARNOUTS S, et al. Halide-guided active site exposure in bismuth electrocatalysts for selective CO_2 conversion into formic acid [J]. Nature Catalysis, 2023, 6(9): 796-806.
[98] AVILA-BOLIVAR B, LOPEZ LUNA M, YANG F, et al. Revealing the Intrinsic restructuring of Bi_2O_3 nanoparticles into Bi nanosheets during electrochemical CO_2 reduction [J]. ACS Appl Mater Interfaces, 2024, 16(9): 11552-11560.
[99] AN X, LI S, HAO X, et al. The in situ morphology transformation of bismuth-based catalysts for the effective electroreduction of carbon dioxide [J]. Sustainable Energy & Fuels, 2020, 4(6): 2831-2840.
[100] LIANG X D, ZHENG Q Z, WEI N, et al. In-situ constructing Bi@$Bi_2O_2CO_3$ nanosheet catalyst for ampere-level CO_2 electroreduction to formate [J]. Nano Energy, 2023, 114:108638.
[101] DETWEILER Z M, WHITE J L, BERNASEK S L, et al. Anodized indium metal electrodes for enhanced carbon dioxide reduction in aqueous electrolyte [J]. Langmuir, 2014, 30(25): 7593-7600.
[102] MA L, LIU N, MEI B, et al. In Situ-activated indium nanoelectrocatalysts for highly active and selective CO_2 electroreduction around the thermodynamic potential [J]. ACS Catalysis, 2022, 12(14): 8601-8609.
[103] HORI Y, KIKUCHI K, SUZUKI S. Production of co and CH_4 in electrochemical reduction of CO_2 at metal electrodes in aqueous hydrogencarbonate solution [J]. Chemistry Letters, 2006, 14(11): 1695-1698.
[104] BACK S, KIM J H, KIM Y T, et al. On the mechanism of high product selectivity for HCOOH using Pb in CO_2 electroreduction [J]. Phys Chem Chem Phys, 2016, 18(14): 9652-9657.

[105] ZHAO C X, BU Y F, GAO W, et al. CO_2 reduction mechanism on the Pb(111) surface: Effect of solvent and cations [J]. The Journal of Physical Chemistry C, 2017, 121(36): 19767-19773.

[106] LEE C H, KANAN M W. Controlling H^+ vs CO_2 reduction selectivity on Pb electrodes [J]. ACS Catalysis, 2014, 5(1): 465-469.

[107] WANG D, ZHANG X, SHEN Y, et al. Ni-doped MoS_2 nanoparticles as highly active hydrogen evolution electrocatalysts [J]. RSC Advances, 2016, 6:16656-16661.

[108] SEH Z W, KIBSGAARD J, DICKENS C F, et al. Combining theory and experiment in electrocatalysis: Insights into materials design [J/OL]. Science, 2017, 355(6321): eaad4998. https://www.science.org/doi/10.1126/science.aad4998.

[109] HONG W T, RISCH M, STOERZINGER K A, et al. Toward the rational design of non-precious transition metal oxides for oxygen electrocatalysis [J]. Energy & Environmental Science, 2015, 8(5): 1404-1427.

[110] MAN I C, SU H Y, CALLE-VALLEJO F, et al. Universality in oxygen evolution electrocatalysis on oxide surfaces [J]. Chem Cat Chem, 2011, 3(7): 1159-1165.

[111] MATTAROZZI L, CATTARIN S, COMISSO N, et al. Electrodeposition of compact and porous Cu-Zn alloy electrodes and their use in the cathodic reduction of nitrate [J/OL]. Journal of the Electrochemical Society, 2015, 162(6): D236-D241. https://iopscience.iop.org/article/10.1149/2.1041506jes.

[112] PANDAY M, UPADHYAY G K, PUROHIT L P. Sb incorporated SnO_2 nanostructured thin films for CO_2 gas sensing and humidity sensing applications [J/OL]. Journal of Alloys and Compounds, 2022, 904: 164053. https://linkinghub.elsevier.com/retrieve/pii/S0925838822004443.

[113] PARK S, KIM W. Advancing electrochemical CO reduction: Insights from operando attenuated total reflectance surface-enhanced infrared absorption spectroscopy analysis [J]. Current Opinion in Electrochemistry, 2024, 45:101515.

[114] REN B, WEN G, GAO R, et al. Nano-crumples induced Sn-Bi bimetallic interface pattern with moderate electron bank for highly efficient CO_2 electroreduction [J/OL]. Nature Communications, 2022, 13(1): 2486. https://www.nature.com/articles/s41467-022-29861-w.

[115] WANG Y, XU A, WANG Z, et al. Enhanced nitrate-to-ammonia activity on copper-nickel alloys via tuning of intermediate adsorption [J/OL]. Journal of the American Chemical Society, 2020, 142(12): 5702-5708. https://pubs.acs.org/doi/10.1021/jacs.9b13347.

[116] ZHENG T, LIU C, GUO C, et al. Copper-catalysed exclusive CO_2 to pure formic acid conversion via single-atom alloying [J/OL]. Nature Nanotechnology, 2021, 16(12): 1386-1393. https://www.nature.com/articles/s41565-021-00974-5.

[117] ZHANG J, WANG X Q, SU T, et al. Calculation of thermic and electric properties and valence electron structure for metallic electrodes of Na‖Sb-Pb-Sn liquid metal battery [J]. Acta Physica Sinica, 2021, 70(8): 83101-83110.

[118] MÁCOVÁ Z, BOUZEK K, ŠERÁK J. Electrocatalytic activity of copper alloys for NO_3 reduction in a weakly alkaline solution: Part 2: Copper-tin [J/OL]. Journal of Applied Electrochemistry, 2007, 37(5): 557-566. https://link.springer.com/10.1007/s10800-006-9287-8.

[119] REN B, WEN G, GAO R, et al. Nano-crumples induced Sn-Bi bimetallic interface pattern with moderate electron bank for highly efficient CO_2 electroreduction [J]. Nat Commun, 2022, 13(1): 2486.

[120] HE J, DETTELBACH K E, HUANG A, et al. Brass and bronze as effective CO_2 reduction electrocatalysts [J]. Angew Chem Int Ed Engl, 2017, 56(52): 16579-16582.

[121] JIANG S, D'AMARIO L, DAU H. Copper carbonate hydroxide as precursor of interfacial CO in CO_2 electroreduction [J]. Chem Sus Chem, 2022, 15: e202102506.

[122] WANG J, ZOU J, HU X, et al. Heterostructured intermetallic CuSn catalysts: High performance towards the electrochemical reduction of CO_2 to formate [J]. Journal of Materials Chemistry A, 2019, 7(48): 27514-27521.

[123] ZENG J, BEJTKA K, JU W, et al. Advanced Cu-Sn foam for selectively converting CO_2 to CO in aqueous solution [J]. Applied Catalysis B: Environmental, 2018, 236:475-482.

[124] JU W, JIANG F, MA H, et al. Electrocatalytic reduction of gaseous CO_2 to CO on Sn/Cu-nanofiber-based gas diffusion electrodes [J]. Advanced Energy Materials, 2019, 9(32): 1901514.

[125] SARFRAZ S, GARCIA-ESPARZA A T, JEDIDI A, et al. Cu-Sn bimetallic catalyst for selective aqueous electroreduction of $CO_2$to CO [J]. ACS Catalysis, 2016, 6(5): 2842-2851.

[126] YAO T, HAN S, XIA W, et al. Atomic indium-doped copper-based catalysts for electrochemical CO_2 reduction to C2+ products [J]. Chem Cat Chem, 2024, 2024:e202400137.
[127] CUI R, YUAN Q, ZHANG C, et al. Revealing the behavior of interfacial water in Te-doped Bi via operando infrared spectroscopy for improving electrochemical CO_2 reduction [J]. ACS Catalysis, 2022, 12(18): 11294-11300.

Research Progress of Operando Spectroscopy for Electrocatalytic CO_2 Reduction

WANG Jun, CHEN Tengfei, JU Wenbo*
(School of Physics and Optoelectronics, South China University of Technology, Guangzhou 510640, China)

Abstract: Electrocatalytic CO_2 reduction reaction (CO_2RR) driven by renewable electricity is able to convert CO_2 to valuable fuels or chemicals, so that it is considered to be a key technique to close the carbon cycle, and to achieve the goals of carbon neutrality. The techno-economic analysis suggests that the production of formic acid (HCOOH) via CO_2RR could generate higher value while consuming less energy. Thus, the CO_2RR to HCOOH has received extensive attention from academia and industry. P-block metals, such as Sn, Bi, In, and Pb, can be used as electrocatalysts for CO_2RR to HCOOH with a high Faradaic efficiency. The understanding of reaction mechanisms and active sites facilitates the development of practicable electrocatalysts and the optimization of the reaction environment. This work summarizes the operando techniques, which have been used to investigating the CO_2RR on p-block metals. The operando techniques include Raman spectroscopy, infrared absorption spectroscopy, X-ray absorption spectroscopy, and differential electrochemical mass spectroscopy. Utilizing in-situ observation technology, we can not only analyze fingerprint information such as chemical bonding, molecular structure, and crystallinity on the catalyst surface, but also conduct qualitative or quantitative analysis of gaseous or volatile products resulting from electrochemical reactions with millisecond time resolution during the potential dynamic scanning process. Through the experimental data obtained under in-situ conditions, the catalytic components of CO_2RR were identified, and the reaction pathway diagram was constructed, laying the groundwork for the further design of high-performance and high-stability catalysts. Additionally, alloying is one of the main strategies to improve the performance of catalysts. In this paper, the effects of p-block metal alloying on electronic structure, surface properties and catalytic effect are briefly discussed. This review emphasizes the importance of operando spectroscopic technology in the research of p-block metal catalysts, and provides a solid foundation and innovative ideas for the engineering development of CO_2RR.

Keywords: p-block metals; CO_2 reduction reaction; formic acid; operando techniques; Raman spectroscopy; infrared absorption spectroscopy; X-ray absorption spectroscopy; differential electrochemical mass spectroscopy

(学术编辑:常成)